New estimation of overland flow velocity based on Manning's equation and equivalent roughness

Youdong Cen (岑由东)[a]; Xiaomin Sun (孙晓敏)[b,*]; Mingwang Zhang (张明旺)[a]; Chenxin Yang (杨晨欣)[a]; Matteo Rubinato[c]; Kuandi Zhang (张宽地)[a]

[a] Key Laboratory of Agricultural Soil and Water Engineering of Ministry of Education in Arid Areas, Northwest A&F University, Yangling, Shaanxi, China

[b] State Key Laboratory of Soil and Water Conservation and Desertification Control, Northwest A&F University, Yangling, Shaanxi, China

[c] Department of Civil Engineering, College of Engineering and Physical Sciences, Aston University, Birmingham, B4 7ET, UK

[*]**Corresponding author:**

Xiaomin Sun, State Key Laboratory of Soil and Water Conservation and Desertification Control, Northwest A&F University, No. 26 Xinong Road, Yangling, Shaanxi 712100, China. Email: sunxiaomin202306@163.com. Tel.: 14 +86-29-18165359636.

Abstract

The overland flow velocity is a fundamental hydraulic variable that directly impacts soil separation, sediment transport, and material deposition during soil erosion. Accurately predicting this velocity is challenging due to the significant spatial variability of overland flow hydraulic characteristics resulting from vegetation covers. To quantify the influence of vegetation stem coverage on mean flow velocity, fixed-bed scouring tests were conducted with eleven stem coverages (0 - 20.42%), four slope gradients (3.49% - 20.78%), and five unit discharges (0.278 - 2.222 $L \cdot m^{-1} \cdot s^{-1}$). The results indicated a trend of mean flow velocity initially increasing and then decreasing as stem coverage rises, with a critical threshold value identified at 2.72%. Compared to studies on bare slopes, an increase in mean velocity ranging from 8.22% to 49.91% was observed on slopes with a stem coverage of 2.72%. The accuracy of velocity prediction can be improved by utilizing both discharge and slope gradient, as opposed to methods that rely solely on unit discharge for prediction. The adjusted correction coefficient (adj. R^2) increased from 0.205 - 0.610 to 0.754 - 0.968. Finally, a dimensionally harmonious flow velocity prediction model based on the adjusted Manning's equation was established using the equivalent roughness, where flow resistance was found to be a combination of grain resistance and stem resistance. The developed model has been proven accurate in predicting experimental results (adj. R^2 = 0.831, Nash-Sutcliffe efficiency coefficient = 0.830). The results obtained here enhance our understanding and prediction of soil erosion, providing further insights into the phenomenon.

Keywords: Mean flow velocity; Manning's equation; Stem coverage; Overland flow; Soil erosion.

1 Introduction

Vegetation plays a pivotal role in mitigating desertification and promoting soil–water conservation in arid and semi-arid regions (Yang et al., 2024; Zhang et al., 2025a). Through the process of vegetation succession, slope morphology is dynamically altered, leading to corresponding changes in the hydrodynamic behavior of overland flow (Li et al., 2022; Cen et al., 2024). These geomorphological and hydrological modifications, in turn, influence water erosion processes by mediating complex interactions among vegetation, surface flow, and sediment transport (Zhao et al., 2025; Zhang et al., 2025b). Among the key parameters in erosion modeling, the mean velocity of overland flow is particularly critical, as it governs the intensity of water erosion, the transport of pollutants, and the generation of slope runoff (Takken et al., 2005; Lima et al., 2015; Pan et al., 2015; Yang et al., 2020). In models such as WEPP (Nearing et al., 1989) and GUEST (Misra and Rose, 1996), mean flow velocity is crucial for calculating runoff power, which is a key predictor of sediment yield. Additionally, mean flow velocity directly impacts soil separation, sediment transport, and deposition processes. Various factors, such as catchment discharge (Govers, 1992), slope (Feng et al., 2020; Liu et al., 2020), and underlying surface conditions (Cen et al., 2023), can alter the spatial and temporal distribution of mean flow velocity, making its prediction challenging. Therefore, a more in-depth exploration of flow velocity prediction methods is necessary,

as accurate measurement is critical for understanding the soil erosion process.

An empirical formula was developed by Govers (1992) to estimate eroded rill flow velocity, which relied solely on the flow discharge in the rill flow.

$$u = \alpha Q^{\beta} \tag{1}$$

Where u represents flow velocity ($m \cdot s^{-1}$), Coefficients α and β are influenced by the morphology of rills, and Q represents flow discharge ($m^3 \cdot s^{-1}$). The power function relationship between u and Q was detailed by Gimenez and Govers (2001), who noted that the fundamental premise for Eq. (1) to hold is that the cross-sectional shape of the rill can dynamically adjust according to the flow conditions. Nearing et al. (2017) also indicated that while u and Q may have a specific functional relationship in rill flow, surface coverage and microtopography in overland flow can affect flow velocity, leading to significant errors in Eq. (1).

To account for the impact of grass coverage on u, Zhang et al. (2017) derived a formula through multiple nonlinear regression analysis by simulating fixed-bed scouring tests under varying vegetation coverage. The resulting formula is expressed as follows:

$$u = 0.35 q^{-0.53Cr+0.63} S^{1.54Cr+0.30} \tag{2}$$

Where q represents the discharge per unit width of the flume ($m^2 \cdot s^{-1}$), Cr represents the grass coverage, and S represents the hydraulic gradient. Eq. (2) quantified the impact of q, Cr, and S on u, noting that the contribution of q to u decreased with increasing Cr, while the contribution of S to u increased. However, Eq. (2) lacks a

theoretical basis and may have significant errors under different surface conditions. Therefore, further research is needed to develop flow velocity calculation formulas with greater applicability.

In surface runoff and erosion models, flow velocity is commonly calculated using Manning's equation (Jarrett, 1984; Mendicino and Colosimo, 2019; Ding et al., 2021). Developed by Robert Manning in 1889, this equation has been crucial in channel flow analysis for over a century and remains a fundamental component of contemporary research (Ferguson, 2010; Mügler et al., 2012). Its expression can be displayed as follows:

$$u = \frac{1}{n} R^{2/3} S^{1/2} \quad . \tag{3}$$

Where R corresponds to the hydraulic radius (m), which is the ratio of the cross-sectional area to the wetted perimeter, and n represents the Manning coefficient ($m^{-1/3} \cdot s$), a roughness index. In the context of overland flow research, n and R are critical factors for evaluating flow resistance and flow performance, respectively. Manning's equation is associated with several assumptions and restrictions, including the requirement of uniform flow, the parallelism between the water surface and the underlying bed, constant flow width, and uniform and random particle roughness on the wetted perimeter (Smith et al., 2007). Although these assumptions limit the use of Manning's equation, some researchers have attempted to correct the Manning coefficient, which can improve the precision of flow velocity estimation for surface runoff. Jin et al. (2000) combined the mechanical equilibrium equation with Manning's

98 equation to obtain the following model:

$$u = \frac{h^{2/3} S^{1/2}}{\left(n_0^2 + \frac{C_d}{2g} D h^{4/3} \right)^{1/2}} \quad . \tag{4}$$

99 Where n_0 represents the Manning coefficient under bare slope conditions ($m^{-1/3} \cdot s$),
100 h represents the depth of overland flow (m), C_d represents the drag coefficient between
101 vegetation and overland flow, D represents the unit density of vegetation, and g denotes
102 the gravitational acceleration ($m \cdot s^{-2}$). The application of Eq. (4) effectively captures the
103 interplay of bed shear stress and vegetation resistance on overland flow dynamics. By
104 assessing the relative contributions of bed surface roughness (n_0) and vegetation factors
105 (C_d and D) to mean flow velocity via Manning's equation, this approach yields valuable
106 insights into the complex interactions between slope hydrology and vegetation. The
107 presented model allows for the accurate determination of overland flow velocity and
108 enables researchers to evaluate the performance of vegetative filter strips in mitigating
109 slope erosion and surface runoff.

110 However, the drag coefficient C_d in Eq. (4) was considered a constant value of 1,
111 and the influence of hydraulic characteristics and vegetation properties on the drag
112 coefficient was not considered. In reality, C_d is influenced by vegetation characteristics
113 such as density (Tanino and Nepf, 2008) and flexibility (Chapman et al., 2015), as well
114 as by the turbulence intensity of flowing water, such as the Reynolds number (Tang et
115 al., 2014). These findings emphasize the importance of considering vegetation features
116 and hydraulic properties when predicting vegetation drag force, which is fundamental

for understanding the behavior of C_d and its implications for the hydraulics of overland flow. Additionally, natural vegetation has complex morphology and distribution patterns, making C_d prediction more difficult (Zhang et al., 2020). Therefore, Eq. (4) needs further refinement to more appropriately evaluate the impact of hydraulic characteristics and vegetation features on C_d.

To comprehensively assess the influence of hydraulic properties, vegetation characteristics, and slope conditions on the Manning coefficient, Fu et al. (2019) carried out a nonlinear regression analysis and developed a new equation incorporating parameters such as plant basal cover, water depth, and slope gradient.:

$$u = \frac{1}{\left(a + b\left(1 - e^{-0.061 C_v}\right)^{1.668}\right) h^{0.604 - 0.710 e^{-0.219 C_v}}} S^{0.5} h^{2/3}. \quad (5)$$

Where C_v represents the plant basal cover, a and b are coefficients. Eq. (5) quantifies the contribution of plant basal cover to the Manning coefficient. However, the model remains somewhat ambiguous in distinguishing the influence of vegetation and bed morphology on flow velocity. Furthermore, the model established based on regression analysis may be affected by test conditions. Parameters a and b vary with the type of vegetation, and the model's applicability to different vegetation types requires adjusting these parameters (Ding et al., 2021). This indicates that a large amount of testing data is needed to fine-tune and verify the parameters of Eq. (5), limiting its broader applicability.

To fill this gap, enhance the precision of overland flow velocity predictions, and

broaden the model's suitability, this research aims to achieve the following objectives: (1) explore the impact of stem coverage on the drag coefficient; (2) develop a novel equation for estimating mean flow velocity under various stem coverages based on the improved Manning's equation of equivalent roughness; and (3) investigate the generality of the proposed flow velocity calculation model. The research results can provide a new method for predicting the velocity of overland flow in environments characterized by vegetation.

2 Materials and methods

2.1 Laboratory devices

The testing setup includes water supply equipment, flume, and flow regulating devices (Fig. 1). The water supply comprises a primary tank (at a constant water level) and a secondary tank that maintains a steady water flow. The water tank measures 2 × 1 × 0.5 meters (length × width × height). To maintain a stable flow in the water tank, two stabilizing grids were placed in the direction of the flow, and an inlet pipe and an outlet pipe were set at both ends of the water tank, respectively. To minimize inlet flow disturbance, a grid was installed within the steady flow water tank located at the inlet of the test flume. This setup ensured reliable and accurate testing of our experimental conditions. Temperature measurements of the steady-flow water tank were taken using a thermometer placed within the tank, with an accuracy of ±0.1 ℃. The experimental flume measures 4.5 × 0.3 × 0.1 meters (length × width × height). To ensure the stability of the experimental flume, a truss support device was positioned beneath it. A slope

157 adjustment device was used beneath the flume to simulate different experimental slope
158 conditions. The flow regulation system employed in this study consisted of valves
159 located on a steady water supply reservoir and a peristaltic pump employed to regulate
160 discharge on a small scale. The adjustable flow range of the valves was 0-90 $L \cdot min^{-1}$,
161 and the adjustable flow range of the peristaltic pump was 0-20 $L \cdot min^{-1}$. These devices
162 played an essential role in maintaining flow stability and accuracy during
163 experimentation.

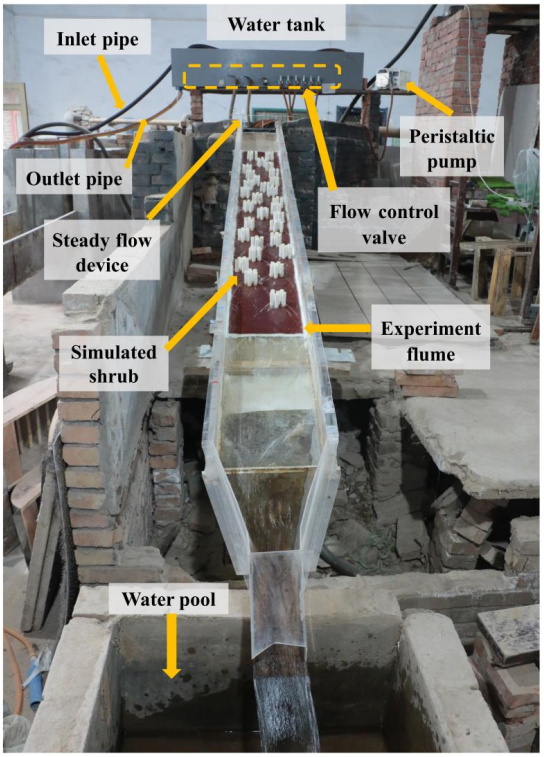

164

165 **Fig. 1.** Diagram of the experimental facility used for this research.

2.2 Experimental Design

To quantitatively explore the impact of vegetation stems on hydraulic characteristics, it is necessary to develop a methodology that mitigates the influence of changes in bed shape on flow. Therefore, this study was conducted under fixed bed conditions. To simulate the presence of vegetation stems, cylinders with a similar flexural rigidity to natural vegetation were used. Each cylinder had a diameter of 17 mm and a height of 60 mm, ensuring that the stems would not be fully submerged during the experiment. Six cylindrical tubes were arranged in a quincunx shape within the test tank.

Wu et al. (2017) reported a median particle size (d_{50}) of 0.38 mm for Loess Plateau loess. To replicate the surface conditions of the Loess Plateau, 40-mesh sandpaper with a roughness of 0.38 mm was affixed to the bottom of the flume. Using sandpaper particles with a size closely resembling the d_{50} of Loess soil allowed for precise recreation of the roughness conditions specific to this region.

Considering the temporal distribution of vegetation coverage, and using the reference from a previous experimental design by Cen et al. (2022), a control group was included alongside ten coverage levels ranging from 2.72% to 20.42% (Fig. 2). These ten coverage levels (2.72%, 5.44%, 8.17%, 10.89%, 13.61%, 14.97%, 16.33%, 17.70%, 19.06%, and 20.42%) ensured a comprehensive evaluation of the effects of varying vegetation coverage levels on flow dynamics.

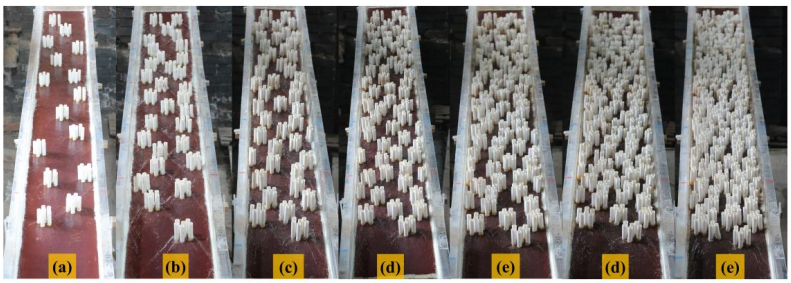

Fig. 2. Schematic diagram of different stem coverages.

In the hydraulic erosion areas of the Loess Plateau, the hydraulic gradient generally does not exceed 26.8% (Cao et al., 2015). Therefore, four slopes of 3.49%, 6.97%, 13.91%, and 20.97% were selected (Table 1) to represent the gentle, moderate, and steep slopes typical of the Loess Plateau.

Table 1. Hydraulic parameters for each hydraulic condition tested.

S	q (L·m^{-1}·s^{-1})	u (m·s^{-1})	h (cm)	Re	Fr
3.49%	0.278	0.089-0.190	0.150~0.371	251.56~359.47	0.47~1.57
	0.556	0.107-0.221	0.259-0.623	501.04-708.27	0.43-1.39
	1.111	0.124-0.259	0.429-1.069	995.94-1382.26	0.38-1.26
	1.667	0.145-0.307	0.543-1.373	1482.95-2029.52	0.42-1.33
	2.222	0.151-0.415	0.550-1.764	1969.98-2647.56	0.36-1.79
6.97%	0.278	0.117-0.220	0.130-0.261	252.17-361.83	0.77-1.95
	0.556	0.122-0.295	0.194-0.543	502.33-713.72	0.53-2.14
	1.111	0.156-0.345	0.331-0.849	998.53-1400.58	0.54-1.91
	1.667	0.193-0.506	0.339-1.049	1488.57-2064.98	0.60-2.77
	2.222	0.204-0.575	0.398-1.333	1975.07-2701.26	0.57-2.91
13.91%	0.278	0.137-0.240	0.119-0.230	252.69-362.55	0.95-2.23
	0.556	0.218-0.344	0.166-0.313	504.04-720.30	1.26-2.69
	1.111	0.243-0.643	0.178-0.546	1001.39-1422.60	1.05-4.88
	1.667	0.281-0.566	0.303-0.721	1494.62-2112.78	1.06-3.29
	2.222	0.292-0.655	0.359-913	1985.27-2786.13	0.98-3.49
20.97%	0.278	0.143-0.213	0.136-0.223	253.01-362.28	0.98-1.81

0.556	0.226-0.374	0.153-0.309	505.00-720.48	1.30-3.06
1.111	0.318-0.477	0.246-439	1004.14-1428.82	1.53-3.07
1.667	0.381-0.549	0.321-550	1499.29-2129.40	1.64-3.09
2.222	0.441-0.698	0.328-0.634	1991.58-2821.99	1.77-3.89

Note: The range of stem coverage is 0~20.42%.

Shang et al. (2020) recorded rainfall measurements ranging from 30 to 120 mm·h^{-1} on the Loess Plateau. For this study, a catchment area of 10 m² and a rainfall duration of 60 minutes were chosen as typical parameters for analysis. Thus, five unit discharges were set for this experimental campaign: 0.278, 0.556, 1.111, 1.667, and 2.222 L·m^{-1}·s^{-1}.

2.3 Experimental measurements

Water depth was the primary parameter observed during the experiments. Four water depth observation sections were longitudinally set along the test flume: 0+1.25m, 0+1.75m, 0+2.25m, and 0+2.75m, from top to bottom. The stem coverage ranged from 0.75m to 3.25m, covering a total area of 0.75 m². Prior to conducting the tests, the design parameters of q, S, and stem coverage were established. The outlet discharge (q) for each trial was measured using the volumetric method within the testing flume. Once the flow rate in the flume stabilized to the designated value, five stable water level measurements were taken at each cross-section to determine the flow depth. Water depth (h) was measured with a water level gauge accurate to ±0.01mm. The mean water depth for each section was calculated as the average of three depth measurements, with maximum and minimum values rounded off. Each section's water depth was sequentially measured, and flow discharge was rechecked after each measurement to

ensure it matched the design parameters.

Throughout the tests, the discrepancy between designed and actual discharge remained within ±5%. If this threshold was exceeded, water depth measurements were repeated. During each measurement, water temperature (t) was carefully monitored using an in-tank thermometer. This data was used to calculate the kinematic viscosity coefficient (υ_0) under specific test conditions. The parameters of q, S, and stem coverage were systematically adjusted for each test run, and this sequence of operations was repeated until all testing was completed. The simulated test data within the experimental facility are presented in Table 1.

2.4 Parameter calculation

The stem coverage (C_s) can be defined as follows:

$$C_s = \frac{N\pi d^2}{4BL}. \tag{6}$$

Where N represents the number of stems tested, d represents the diameter of the stems (0.017m), B represents the width of the experimental flume (0.3m), and L denotes the length of the vegetated distribution area, which was 2.5 m.

The calculation for the u is expressed as follows:

$$u = \frac{q}{hB_1}. \tag{7}$$

Where B_1 represents the useful channel width during the testing (m), $B_1 = B \times (1 - C_s)$.

The Reynolds number Re is defined as follows:

$$Re = \frac{uR}{v}. \tag{8}$$

Where v is the kinematic viscosity and can be computed by the Poiseuille formula as follows:

$$\nu = \frac{0.01775}{\left(1 + 0.0337t + 0.00022t^2\right)} \tag{9}$$

The Froude number Fr can be estimated by the Eq. (10) presented below:

$$Fr = \frac{u}{\sqrt{gh}} \tag{10}$$

2.5 Metrics for evaluating model performance

To evaluate the model's performance, we utilized three parameters: the adjusted correlation coefficient (adj. R^2), Nash-Sutcliffe efficiency coefficient (*NSE*), relative error (*RE*), and relative root mean square error (*RRMSE*). The evaluation standards for these parameters are shown in Table 2.

Table 2. Metrics for evaluating model performance

No.	parameter	The formula for calculating parameters	Evaluation criteria
11	R^2	$R^2 = \frac{\left[\sum_{i=1}^{n}(O_i - O_m)(P_i - P_m)\right]^2}{\sum_{i=1}^{n}(O_i - O_m)^2 \sum_{i=1}^{n}(P_i - P_m)^2}$	The performance of the model is better when its value approaches closer to 1.
12	adj. R^2	$\text{adj.}R^2 = 1 - \frac{n-1}{n-p-1}(1-R^2)$	
13	*NSE*	$NSE = 1 - \frac{\sum_{i=1}^{n}(O_i - P_i)^2}{\sum_{i=1}^{n}(O_i - O_m)^2}$	
14	*RRMSE*	$RRMSE = \frac{\sqrt{(1/n)\sum_{i=1}^{n}(O_i - P_i)^2}}{O_m}$	The performance of the model is

			better when its value approaches closer to 0.
15	*RE*	$RE = \frac{O_i - P_i}{O_i}$	The model uncertainty decreases asymptotically as the *RE* approaches zero.

Note: O_i and O_m represent the measured and mean observed values of the flow velocity, while P_i and P_m denote the predicted and mean predicted values of the flow velocity. The variables n and p represent the number of observed flow velocities and independent variables, respectively.

2.6 Theoretical analysis

The hydraulic characteristics and the stress of the surface runoff on the natural slope are complex to quantify due to vegetation disturbance. Therefore, the equivalent roughness method was used to simplify the problem effectively. This method assumes that the resistance posed by bare rough beds is equivalent to that of vegetated stems, attributing the form resistance of stems with a similar effect as the shear stress from underlying rough surfaces lacking vegetation. Previous investigations have documented the use of this method (Kim et al., 2012; Wang et al., 2015; Cen et al., 2023). Mechanical analysis results indicated that drag force from stems (F_D) obstructed overland flow in the direction of movement, while shear stress from bed surface roughness (F_b) also impeded flow. Conversely, gravity (F_G) facilitated downward flow movement (Fig. 3a).

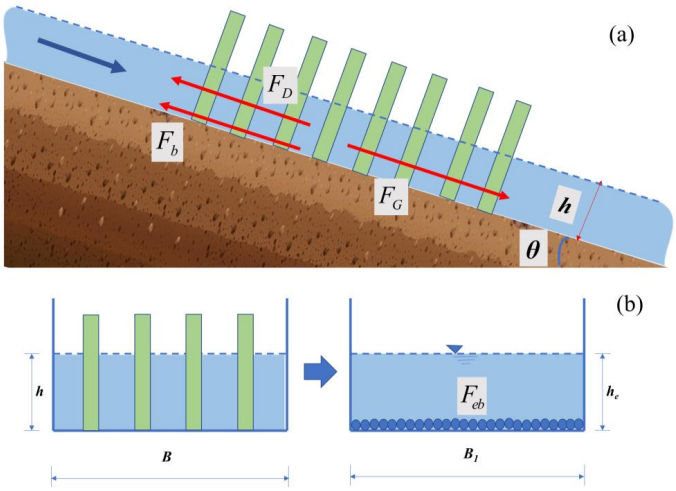

Fig. 3. Forces diagram (a), and schematic of the equivalent roughness (b).

According to the mechanical analysis, the following equation can then be considered:

$$F_b + F_D = F_G \tag{16}$$

The equations needed to estimate F_b and F_D can be written as follows:

$$F_b = \gamma RSB_1L = \frac{\gamma u^2 n_0^2}{R^{1/3}} B_1L \tag{17}$$

$$F_D = \frac{\gamma C_d A_i u^2}{2g} \tag{18}$$

Where γ signifies the unit weight of the liquid being analyzed (N/m^3), and A_i represents the obstructed cross-sectional area of vegetation in the direction of flow (m^2), A_i=Ndh.

By applying the equivalent roughness method, the flow resistance caused by

263 vegetation stems was evenly distributed across the channel bed, leading to an equivalent
264 water flow shear stress in the channel cross-section, as depicted in Fig. 3b.

265 The controlled water volume of the vegetation arrangement before and after
266 equivalence was quantified as follows:

$$V = BLh\left(1-C_s\right), \tag{19}$$

$$V_e = BLh_e . \tag{20}$$

267 Before equivalence, V denotes the water volume regulated in the areas covered by
268 stems (m^3), V_e represents the controlled water volume in these areas after equivalence
269 (m^3), and h_e denotes the flow depth in the equivalent cross-section (m). The principle
270 of fluid mass conservation ensures that the water volume regulated in stem-covered
271 areas remains unchanged both before and after equivalence. Eq. (19) and Eq. (20) are
272 then solved as follows:

$$h_e = h\left(1-C_s\right) \tag{21}$$

273 The flow discharge before and after equivalence is as follows:

$$u_e h_e B = uhB_1 \tag{22}$$

274 Eq. (21) and Eq. (22) can be combined, leading to Eq. (23):

$$u_e = u \tag{23}$$

275 After cross-sectional equivalence, the equivalent bed shear stress (F_{eb}) induced by
276 the equivalent bed roughness can be determined using the following equation:

$$F_{eb} = \gamma R_e SBL = \frac{\gamma u_e^2 n_e^2}{R_e^{1/3}} BL \tag{24}$$

Where R_e and n_e represent the hydraulic radius and Manning coefficient after equivalence, respectively. In accordance with the mechanical balance equation, the equivalent bed shear stress was balanced by the gravitational forces governing the fluid motion, which can be mathematically expressed as:

$$F_{eb} = F_G \tag{25}$$

The simultaneous Eqs. (16) and (25) are solved, namely:

$$F_{eb} = F_b + F_D \tag{26}$$

$$\frac{\gamma u_e^2 n_e^2}{R_e^{1/3}} BL = \frac{\gamma u^2 n_0^2}{R^{1/3}} B_1 L + \frac{\gamma C_d N d h u^2}{2g} \tag{27}$$

The solution is simplified as follows:

$$n_e = \sqrt{(\frac{R_e}{R})^{1/3} n_0^2 (1 - C_s) + R_e^{1/3} C_d \frac{2hC_s}{\pi dg}} \tag{28}$$

Substitute Eq. (28) into Eq. (3) and simplify it to obtain:

$$u = \frac{kR^{1/2} S^{1/2}}{\sqrt{\frac{n_0^2 (1 - C_s)}{R^{1/3}} + C_d \frac{2hC_s}{\pi dg}}}, \tag{29}$$

Where k is the coefficient, and C_d needs to be determined according to the experimental conditions. From the perspective of dimensional analysis, Eq. (29) is dimensionally consistent, demonstrating the correctness of the structure of Eq. (29).

3 Results

3.1 The relationship between u and C_s

Under all tested conditions, the relationship between u and C_s exhibited an initial increase followed by a subsequent decrease, with the rate of change influenced by the slope gradient (Fig. 4). Compared to the bare slope condition (C_s = 0), on slopes with C_s = 2.72%, u increased by 15.14% - 85.53%, 44.82% - 87.17%, 32.47% - 75.47%, and 35.29% - 38.30% under slope gradients of 3.49%, 6.97%, 13.91%, and 20.97%, respectively. This indicates that the rate of change becomes more uniform with steeper slope gradients. An inverse relationship between u and C_s was observed when C_s exceeded 2.72%, indicating a reduction in u at higher C_s values. For instance, compared to C_s = 2.72%, when C_s = 20.42%, u decreased by 46.27% - 59.59%, 34.13% - 63.54%, 31.29% - 45.47%, and 25.15% - 36.83% for the four slope gradients, respectively, showing a smaller reduction rate with steeper slopes.

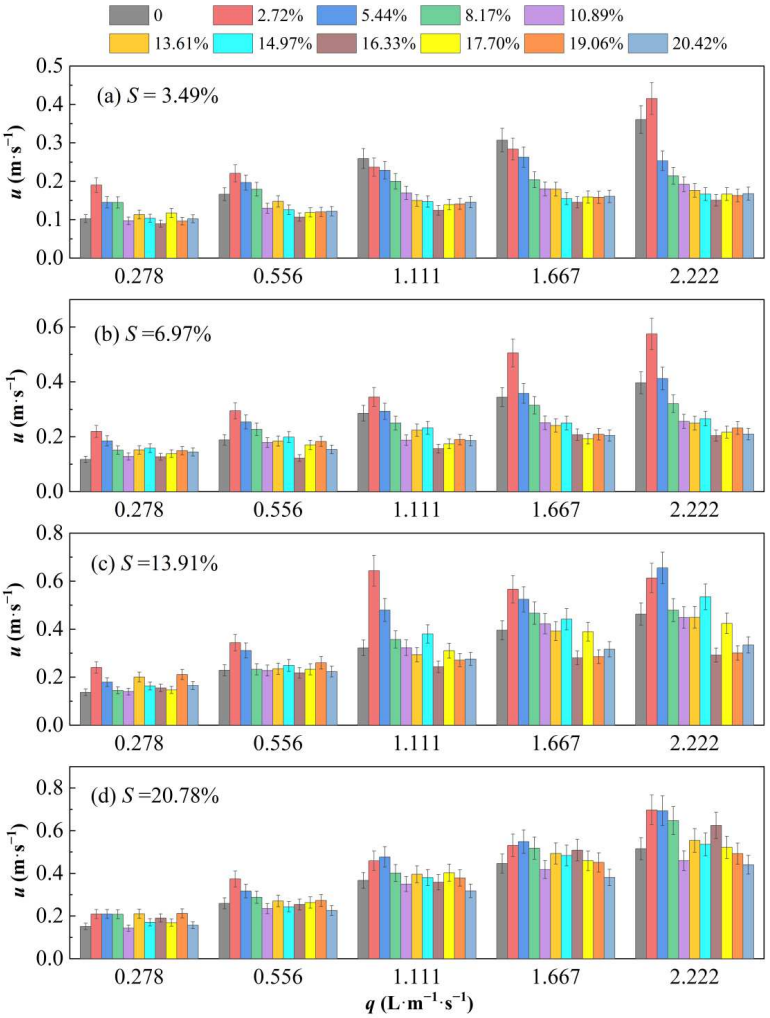

Fig. 4. Relationship between flow velocity and stem coverage under different slope gradients and unit discharges.

The influence of C_s on u is more pronounced with increased unit discharge. Across the four slope gradients, an increase in unit discharge from 0.278 to 2.222 L·m^{-1}·s^{-1}

resulted in mean flow velocity increases ranging from 68.39% to 148.92%, 73.93% to 160.71%, 113.28% to 138.44%, and 207.07% to 207.42%, respectively. This illustrates that steeper slope gradients lead to greater increases in flow velocity.

3.2 The variation pattern of *u* under different *q* and *S* conditions

An increase in both q and S led to an upward trend in u, with the growth rate observed to be influenced by stem coverage (Fig. 5). Under bare slope conditions, as q increased from 0.278 to 2.222 $L \cdot m^{-1} \cdot s^{-1}$, u ranged from 0.103-0.152 to 0.361-0.516 $m \cdot s^{-1}$, demonstrating a strong power function relationship between mean flow velocity, q, and S. On the slope with C_s = 8.17%, as q increased from 0.278 to 2.222 $L \cdot m^{-1} \cdot s^{-1}$, u changed from 0.145-0.209 to 0.214-0.617 $m \cdot s^{-1}$. Except for slopes with gradients of 3.49% and 6.97%, u values under all conditions were higher than those under bare slope conditions.

Vegetation cover moderated the growth rate of u with q when slope gradient S was less than 6.97%, but accelerated it when S was greater than 6.97%. Similar trends were observed on slopes with C_s = 10.89% and C_s = 13.61%. On slopes with C_s = 16.33% and C_s = 20.42%, mean flow velocities under all conditions were lower than those under bare slope conditions, with reductions ranging from 89.15% to 93.48% and 70.59% to 68.05%, respectively. These findings indicate that increasing C_s inhibited the growth of u triggered by q and S.

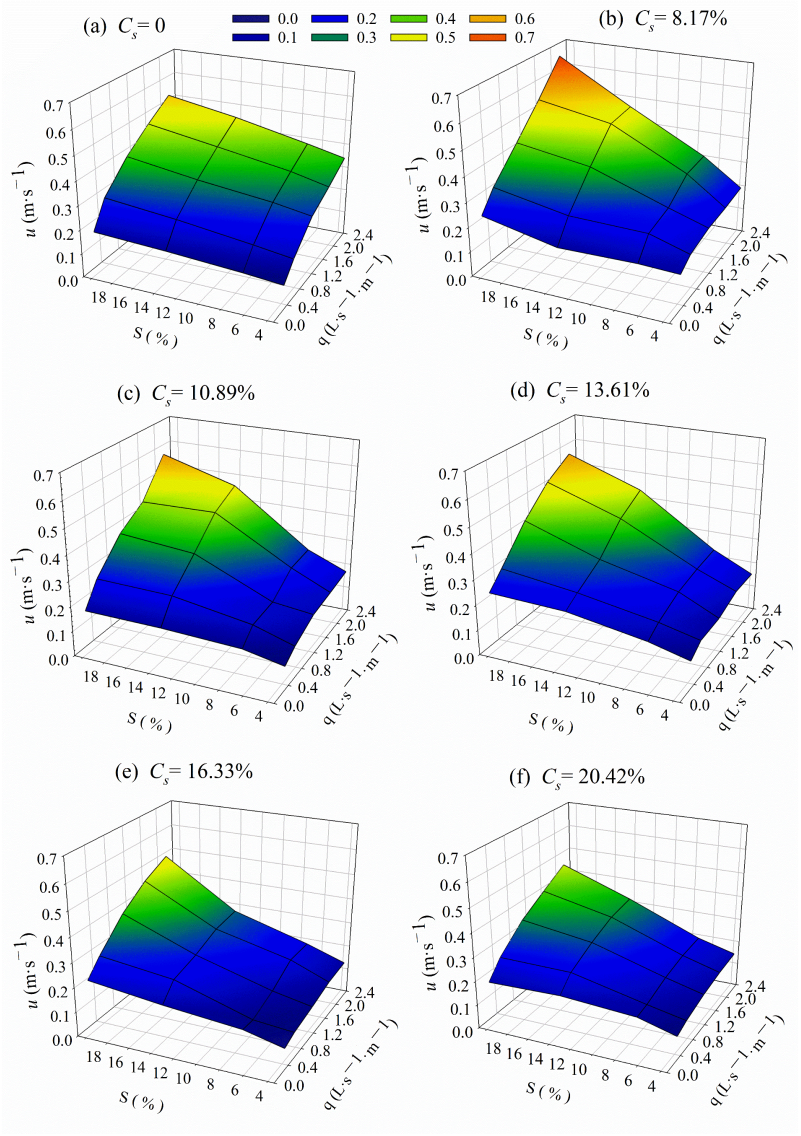

Fig. 5. The relationship between mean flow velocity, unit discharge, and slope gradients under different stem coverage.

To investigate whether u was independent of S and whether it could be predicted solely by q, predictions of u using only q were compared with predictions using both q and S (Table 3). When only q was used, the exponent range for q was 0.397-0.551. When q and S were both used, the exponent range for q was 0.412-0.549, which remained close to 0.5, while the exponent range for S was 0.211-0.796. For the slope with C_s = 0, u could be predicted using only q (adj. R^2 = 0.859). However, under conditions with vegetation cover, using only q to predict u resulted in unacceptable errors. Experimental results demonstrated that considering the effect of S improved the accuracy of u prediction, with adj. R^2 increasing from 0.205-0.610 to 0.754-0.968. To establish an accurate prediction model for u, the influence of S on u must be carefully considered.

Table 3. Fitting equations of the mean flow velocity, unit discharge, and slope gradient for different stem coverage.

Stem coverage	Fitting equation	adj.R^2	Fitting equation	adj.R^2
0	$u = 0.283q^{0.551}$	0.859	$u = 0.463q^{0.549}S^{0.211}$	0.993
2.72%	$u = 0.393q^{0.452}$	0.610	$u = 0.756q^{0.456}S^{0.282}$	0.861
5.44%	$u = 0.344q^{0.467}$	0.508	$u = 0.927q^{0.496}S^{0.436}$	0.947
8.17%	$u = 0.294q^{0.445}$	0.454	$u = 0.877q^{0.487}S^{0.486}$	0.953
10.89%	$u = 0.244q^{0.450}$	0.476	$u = 0.689q^{0.474}S^{0.457}$	0.940
13.61%	$u = 0.264q^{0.376}$	0.326	$u = 0.941q^{0.412}S^{0.566}$	0.968
14.97%	$u = 0.266q^{0.441}$	0.371	$u = 0.915q^{0.482}S^{0.549}$	0.926
16.33%	$u = 0.226q^{0.418}$	0.244	$u = 1.279q^{0.476}S^{0.796}$	0.905
17.70%	$u = 0.244q^{0.397}$	0.312	$u = 0.976q^{0.440}S^{0.622}$	0.956
19.06%	$u = 0.240q^{0.269}$	0.205	$u = 0.889q^{0.291}S^{0.582}$	0.940
20.42%	$u = 0.222q^{0.340}$	0.353	$u = 0.663q^{0.368}S^{0.484}$	0.960

3.3 Flow regimes under different stem coverage

According to Table 4, the flow regime of overland flow can be classified into different categories based on varying *Fr* and *Re* ranges, with detailed information available in Cen et al. (2023).

Table 4. Classification criteria for overland flow regimes.

Fr	*Re*		
	Re<580	580<*Re*<5000	*Re*>5000
Fr<1	subcritical laminar flow	subcritical transitional flow	subcritical turbulent flow
Fr>1	supercritical laminar flow	supercritical transitional flow	supercritical turbulent flow

Based on the principles discussed above, the flow regimes under various experimental conditions are illustrated in Fig. 6. Within the range of 0.278 - 2.222 $L \cdot m^{-1} \cdot s^{-1}$, the flow did not reach the turbulent zone, and the transition from laminar to transitional flow was primarily influenced by the unit discharge. For C_s < 13.61%, a discharge of $q = 0.556\ L \cdot m^{-1} \cdot s^{-1}$ marked the critical point for the transition from laminar to transitional flow. When C_s > 13.61%, the critical discharge was less than 0.556 $L \cdot m^{-1} \cdot s^{-1}$, indicating a positive correlation between *Re* and increasing C_s.

As the slope gradient *S* increased, there was a transition in flow regime from subcritical to supercritical, corresponding to an increase in *Fr*. Flow conditions were identified as supercritical for *S* values of 13.91% and higher. With increasing C_s, the flow regime shifted towards subcritical, signifying a decrease in *Fr*. On a slope with *S* = 3.49%, flow was supercritical when C_s was < 5.44%. At *S* = 6.97% slope, the flow transitioned from subcritical to supercritical when C_s reached a critical coverage of 14.97%.

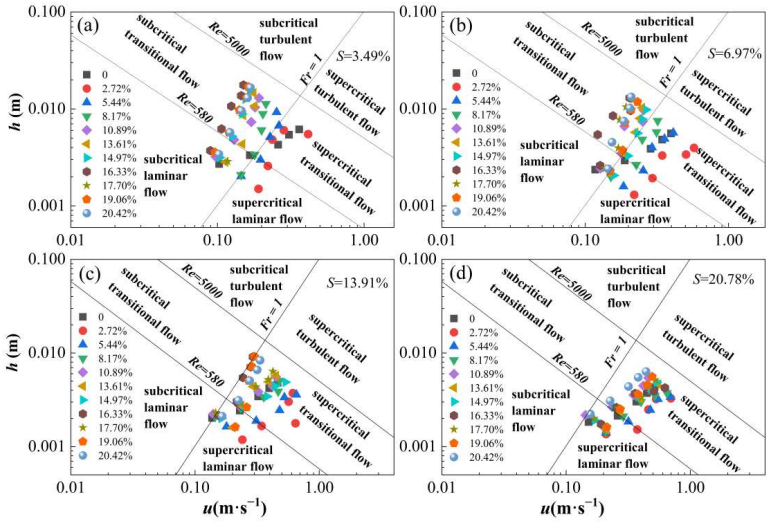

Fig. 6. Flow regimes under different stem coverage and slope gradients tested.

In summary, the transition from laminar to transitional flow was predominantly governed by unit discharge, while the shift from subcritical to supercritical conditions was influenced by both stem coverage and slope gradient.

3.4 Establishment of the formula for calculating mean flow velocity

The experimental dataset was partitioned into two equal subsets for model development and predictive accuracy validation. Furthermore, the model was further validated against external datasets from Fu et al. (2019) and Han et al. (2021) to assess its generalizability. Subsurface conditions, hydraulic parameters, and vegetation characteristics across all datasets are summarized in Table 5. Notably, the present study and Fu et al. (2019) employed fixed-bed configurations with clear-water flow, whereas Han et al. (2021) utilized mobile-bed conditions with sediment-laden flow,

372 featuring *Pittosporum tobira* and *Ophiopogon japonicus* as vegetation cover. These
373 datasets collectively represent diverse topographic features, hydrodynamic regimes,
374 and vegetation heterogeneities.

375 As illustrated in Fig. 7, validation data points clustered tightly around the 1:1 line.
376 Statistical evaluations revealed adj.R^2 of 0.831, 0.971, and 0.713, *NSE* of 0.830, 0.978,
377 and 0.691, and *RRMSE* of 0.204, 0.135, and 0.081 for the current study, Fu et al. (2019),
378 and Han et al. (2021) datasets, respectively. These results demonstrate broad
379 applicability of the proposed model across both fixed-bed clear-water and mobile-bed
380 sediment-laden flow environments.

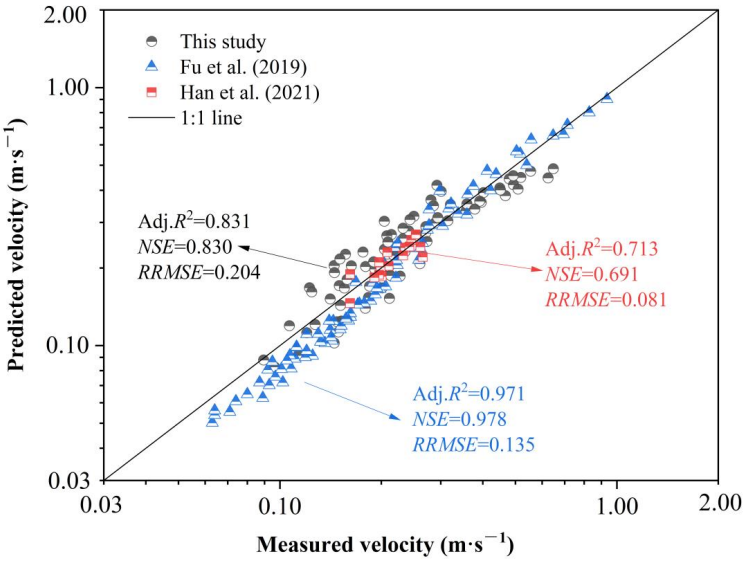

381
382 **Fig. 7.** Validation of the mean flow velocity model.

383 **Table 5**. Statistical parameters of different datasets

Date set	Bed type (M = mobile; F = fixed)	Flow condition	Vegetation type	Scope of Re	k	C_d	Scope of C_d	Adj.R^2	NSE	$RRMSE$	N
This study	F	Sediment-free flow	Rigid cylinder	318-2821	2.053	$C_d = \frac{4905.86}{Re^{0.890}}$	4.17-29.08	0.831	0.830	0.204	80
Fu et al. (2019)	F	Sediment-free flow	Artificial Gramineae stems	1445-6278	1.006	$C_d = \frac{2434.20}{Re^{0.535}}$	22.62-49.64	0.971	0.978	0.135	81
Han et al. (2021)	M	Sediment-laden flow	*Pittosporum tobira* and *Ophiopogon japonicus*	19-90	1.932	$C_d = \frac{9.19}{Re^{0.034}}$	10.15-10.71	0.713	0.691	0.081	16

384 Note：N is the number of samples in the dataset.

Relative error (*RE*) was employed to quantify prediction uncertainty across datasets (Fig. 8). For the dataset of this study, model outputs exhibited both overestimations (RE_{min}= −0.487) and underestimations (RE_{max} = 0.294) at u < 0.38 m·s^{-1}, whereas systematic underestimation occurred (RE_{max} = 0.283) when u exceeded this threshold. The Fu et al. (2019) dataset demonstrated underestimation (RE_{max} = 0.296) at u < 0.20 m·s^{-1}, shifting to predominant overestimation (RE_{min} = −0.335) at higher velocities. In contrast, the Han et al. (2021) dataset displayed balanced prediction deviations (RE_{max} = 0.171; RE_{min} = −0.169) across all velocity ranges.

Aggregate statistical analysis revealed mean *RE* values (μ) of −0.035, 0.098, and 0.005 with corresponding standard deviations (*SD*) of 0.198, 0.130, and 0.081 for the present study, Fu et al. (2019), and Han et al. (2021) datasets, respectively.

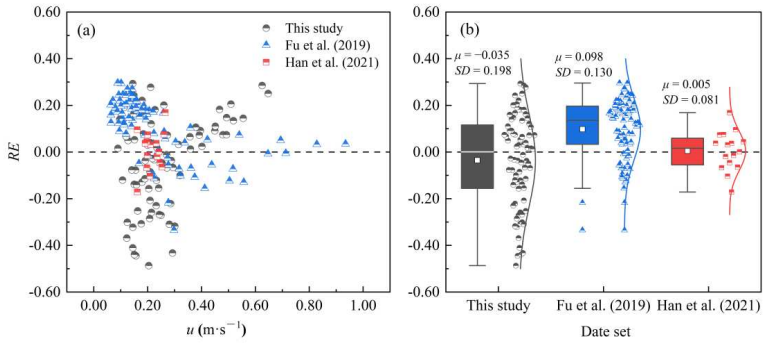

Fig. 8. Error analysis of the mean flow velocity model on different datasets.

4 Discussion

4.1 The non-monotonic relationship between *u* and C_s

In the current study, plastic cylinders simulated rigid vegetation stems to

401 investigate the effect of C_s on u. The findings revealed a non-monotonic relationship
402 between u and C_s, with u initially increasing and subsequently decreasing as stem
403 coverage increased under all scenarios (Fig. 4). The critical stem coverage was found
404 to be 2.72%. Previous research (Bouma et al., 2007) noted that u tends to increase with
405 low vegetation coverage compared to bare slopes (C_s = 0). Bouma et al. (2007)
406 suggested that the relationship between u and patch density is not constant, showing
407 higher erosion around low-density vegetation patches than high-density ones, which
408 aligns with findings by Van et al. (2008) in field experiments. Zong and Nepf (2010)
409 observed increased turbulence activity in patches with low stem density. Ban et al.
410 (2017) found a positive relationship between flow velocity and coverage when gravel
411 coverage was below 10%, and a negative correlation otherwise, further confirming the
412 non-constant relationship between flow velocity and surface cover.

413 The protrusion of plant structures from the flow surface alters the local flow field,
414 impacting hydraulic erosion processes (Friedrich et al., 2000). Previous studies have
415 shown that flow velocity gradually decreases as coverage increases (Pan and
416 Shangguan, 2006; Mu et al., 2019). Discrepancies in the flow velocity and coverage
417 relationship could stem from variations in vegetation cover levels and measured
418 discharge. Pan and Shangguan (2006) used rainfall simulators to simulate surface runoff
419 scouring, where flow velocity was affected by raindrop impact on the ground. In
420 contrast, our study examined lower stem cover and discharge compared to Mu et al.
421 (2019), revealing new insights into vegetation coverage's role in governing runoff

velocity, particularly under low discharge conditions.

Our study identified a two-stage relationship between u and C_s. Initially, under low coverage scenarios, vegetation minimally affects overland flow resistance (Fig. 9), while reducing the channel's cross-sectional area accelerates flow. Subsequently, as vegetation coverage increases, drag force on the flow (Zhang et al., 2022b) amplifies water depth and diminishes flow velocity. In summary, our findings demonstrate a non-constant relationship between flow velocity and coverage on non-erosion slopes, significantly influenced by S and q.

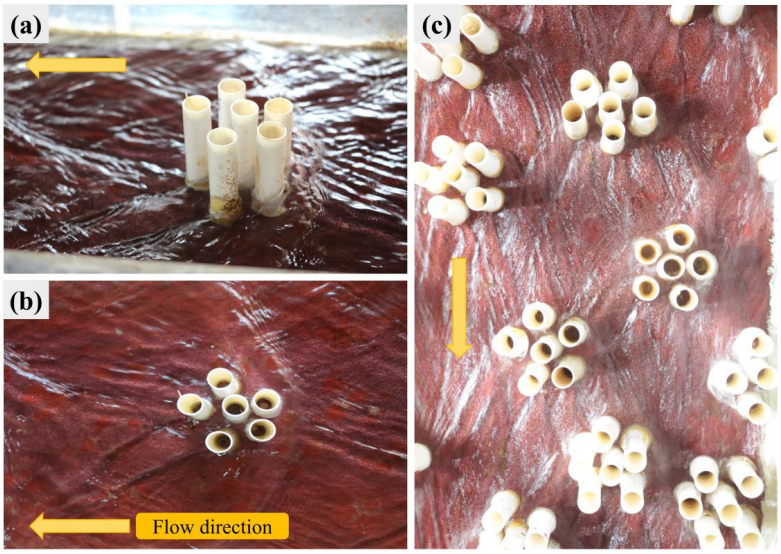

Fig. 9. The hydraulic characteristics under different coverage, (a) and (b) have a coverage of 2.72%, and (c) have a coverage of 10.89%.

4.2 Response of u to changes in S under different bed conditions

The relationship between u and S under different stem coverages was investigated in this study. It was observed that u and S exhibited a positive correlation (Fig. 5).

436 Incorporating both *S* and *q* improved the prediction accuracy of *u* compared to using q
437 alone. This finding contradicts the conclusion that slope gradient can independently
438 predict mean flow velocity using discharge alone (Hessel et al., 2003). According to
439 Hessel et al. (2003), increases in *S* led to negligible changes in *u*, despite steeper rill
440 flow gradients promoting channelization and exacerbating rill erosion.

441 Nearing et al. (2017) demonstrated that steep slopes with initially elevated flow
442 velocities tend to develop enhanced surface roughness through erosional processes,
443 thereby inducing progressive attenuation of flow momentum. Polyakov et al. (2018)
444 demonstrated that *u* on grasslands was primarily influenced by *q*, showing no clear
445 correlation with *S* or soil characteristics, attributing this to the dynamic feedback
446 between *u* and slope shape on erodible slopes.

447 Differences between this study and prior research can be attributed to experimental
448 methodology. In this study, the underlying surface shape remained constant and did not
449 respond to changes in *u*. As *S* increased, the gravitational component of flow increased,
450 enhancing its kinetic energy through gravity-induced mechanical work, thereby
451 increasing velocity.

452 The results underscore the necessity of considering the effect of *S* on *u* when the
453 bed shape does not respond to hydraulic characteristics. Increasing *S* improved the
454 accuracy of predicting mean flow velocity. Variations in slope gradient can create
455 heterogeneous flow resistance, influencing flow velocity fluctuations. David et al.
456 (2010) emphasized the critical role of slope gradient in shaping slope geometry and

457 altering overall flow resistance distribution. Rickenmann and Recking (2011) also
458 highlighted the importance of including S in models to explain changes in flow
459 resistance across different locations.

460 Furthermore, when both q and S were used to predict u, the exponent range of q
461 was found to be 0.412-0.549. Similarly, Comiti et al. (2007) reported an exponent range
462 of 0.48-0.6 characterizing the relationship between u and q in steep-gradient streams.
463 These findings underscore the significance of S in predicting flow velocity when bed
464 surface conditions are relatively stable, highlighting that considering the S factor
465 enhances prediction accuracy of u.

466 **4.3 Analysis and Evaluation of a Novel Velocity Equation for Overland**
467 **Flow under Vegetation-Modified Slope Conditions**

468 The Manning's equation was enhanced through integration of equivalent
469 roughness theory and mechanical equilibrium principles, demonstrating improved
470 predictive performance. Statistical evaluations of the experimental dataset revealed
471 adj.R^2 and NSE exceeding 0.8. To address vegetation-induced variability in drag
472 coefficients (Chapman et al., 2015), vegetation-specific formulations for drag
473 coefficient calculation and k-values were developed (Table 5). For the Fu et al. (2019)
474 dataset, the enhanced model achieved adj.R^2 and NSE values exceeding 0.9. For the
475 Han et al. (2021) dataset, adj.R^2 and NSE values exceeded 0.65 despite experimental
476 conditions involving mobile-bed sediment-laden flows and natural vegetation cover
477 (*Pittosporum tobira* and *Ophiopogon japonicus*). Therefore, although calibration data

were obtained from fixed-bed and sediment-free flow experiments, the model's adaptive parameterization of Manning's coefficient enables effective adaptation to dynamic topography, sediment transport, and vegetation heterogeneity.

Error analysis revealed heightened predictive uncertainty at low flow velocities. For the current dataset, elevated RE variability (RE_{max} = 0.294; RE_{min} = −0.487) was observed at u < 0.38 m·s^{-1}, while the Fu et al. (2019) dataset exhibited systematic underestimation (RE_{max} = 0.296) below u = 0.20 m·s^{-1}. These low-velocity discrepancies are attributed to hydrodynamic interactions with dense vegetation coverage and complex slope morphology, where vegetation-induced flow separation phenomena dominate (Fig. 9). Spatial heterogeneity in velocity distribution arises from contrasting flow patterns at vegetation stems (lower velocities) versus interstitial zones (accelerated flows). Discrepancies in critical velocity thresholds between studies likely stem from divergent experimental conditions in vegetation types and discharge ranges (Table 5). The Han et al. (2021) dataset exhibited a near-Gaussian distribution of RE (Fig. 8b), with model uncertainty likely originating from the coupled complexities of dynamic topography and sediment transport processes. When extrapolating beyond calibration conditions (fixed-bed sediment-free flows), parameter recalibration is recommended to mitigate error propagation.

The developed framework establishes a dynamic parameterization system for flow resistance quantification. In overland flow scenarios, surface resistance components exhibit nonstationary behavior, particularly under laminar flow regimes (Helmers and

499 Eisenhauer, 2006). Treating Manning's coefficient as a constant may induce parameter
500 overfitting and computational artifacts (Shen et al., 2021; Cen et al., 2023),
501 fundamentally limiting the applicability of Manning's equation to hillslope hydraulics
502 (Kirstetter et al., 2016). Field observations confirm the discharge-dependent nature of
503 flow resistance in overland systems, characterized by dynamic feedback between
504 hydraulic forces and boundary conditions (Polyakov et al., 2018; Liu et al., 2023).
505 Caution is warranted when applying fixed Manning's coefficient values, given their
506 documented inverse correlation with flow magnitude (Ferguson et al., 2021). By
507 dynamically coupling Manning's coefficient with substrate characteristics and
508 hydrodynamic parameters, this framework elucidates the mechanistic origins and
509 spatiotemporal evolution of flow resistance.

510 Eq. (29) demonstrates three critical advancements compared to prior formulations.
511 First, unlike Eq. (1), it explicitly resolves vegetation-induced flow retardation through
512 roughness-vegetation coupling mechanisms. Second, in contrast to Eq. (4), it
513 establishes a vegetation-adaptive drag coefficient framework applicable to
514 heterogeneous canopy cover conditions. Third, building upon Eq. (5), it decomposes
515 Manning's coefficient into grain resistance (substrate roughness-driven) and form
516 resistance (roughness element-induced), quantitatively linking vegetation
517 characteristics to hydrodynamic responses. This formulation captures resistance
518 variability arising from dynamic substrate roughness, vegetation heterogeneity, and
519 hydrodynamic parameter shifts, thereby overcoming theoretical constraints in

conventional approaches. However, model accuracy diminishes under conditions involving coupled morphodynamic adjustments and sediment transport processes (Table 5). Future implementations should integrate quantitative sediment-flux and bedform evolution modules to extend applicability to transient fluvial environments.

4.4 Limitations and Prospects

Theoretically, this investigation was conducted under fixed-bed, non-erodible conditions, with water-sand cloth (equivalent roughness $k_s = 0.38$ mm) replicating loess surface roughness (Wu et al., 2017). While this approach minimized measurement errors in flow depth and velocity, it inherently excluded dynamic feedback mechanisms between flow, sediment transport, and topography observed in natural erosion processes. In field settings, sediment transport redistributes flow energy, modifying vertical velocity profiles (Li and Abrahams, 1997)—a phenomenon unrepresented in fixed-bed experiments. Furthermore, steep-slope environments often exhibit rill development and dynamic bedform adjustments due to erosion, which amplify form drag and alter the universality of velocity-slope relationships (Nearing et al., 2017). The current model's exclusion of such morphodynamic coupling may constrain its applicability to steep-slope erosional landscapes. Future validation under complex field conditions, particularly scenarios integrating multiscale roughness elements and topographic evolution, is essential to delineate the model's operational boundaries in dynamic environments.

Practically, laboratory-scale simulations of natural roughness face inherent scaling

541 constraints. Natural slopes exhibit multiscale roughness elements (e.g., rock fragments,
542 litter, biocrusts) with spatial heterogeneity influencing vertical velocity distributions
543 through wake interference and turbulent bursting (Ali et al., 2012; Zhang et al., 2023;
544 Wei et al., 2024). The absence of these microtopographic features in controlled
545 experiments likely underestimates natural flow resistance variability. Additionally, rigid
546 cylindrical analogs for vegetation stems, while replicating stiffness-induced flow
547 resistance, neglect bending deformation effects of flexible natural vegetation (e.g.,
548 grasses, shrubs). Such deformation reduces effective flow-blocking areas, potentially
549 diminishing hydrodynamic drag forces (Li et al., 2024). Subsequent studies should
550 employ natural vegetation prototypes to quantify flexibility-induced modifications to
551 flow velocity fields.

552 ## 5 Conclusions

553 This study presented a new method for predicting overland flow velocity by
554 integrating Manning's equation with an equivalent roughness framework. Using fixed-
555 bed flume experiments, the influence of vegetation stem coverage on flow velocity was
556 quantified across a range of slope gradients and unit discharges. The key outcomes can
557 be summarised as follows:

558 (1) Flow velocity (u) showed a unimodal response to stem coverage (C_s),
559 increasing up to a critical threshold (2.72%) and decreasing thereafter. At C_s = 2.72%,
560 flow velocity improved by 8.22%–49.91% relative to bare slopes.

561 (2) Including slope gradient in predictive equations significantly improved model

accuracy. Adj. R^2 values rose from 0.205–0.610 (using discharge only) to 0.754–0.968 (using both slope and discharge).

(3) The proposed velocity prediction model, derived from an improved Manning's equation and equivalent roughness principles, achieved high performance (adj.R^2 > 0.8, NSE > 0.8) for the experimental data. It also demonstrated good generalizability when validated against external datasets.

While the model performs well under controlled conditions, future work should incorporate morphodynamic feedbacks, sediment transport coupling, and flexible vegetation structures to capture the complex interactions present in natural slope environments. In particular, in situ validation under transient rainfall events and evolving topographies is essential for operational deployment of the framework in landscape-scale erosion assessments.

Data Availability

All data used during the study are available from the corresponding author by request.

Conflict of Interest

The authors declare no conflicts of interest relevant to this study.

Acknowledgments

This research was financially supported by the National Natural Science Foundation of China [grant numbers 52179079, 41877076]; Inner Mongolia Department of Science and Technology 2024 major projects to prevent and control sand demonstration 'unveiled marshal' project [grant number 2024JBGS0016]; Shaanxi Provincial Water

583 Conservancy Science and Technology Plan Project [grant number 2023slkj-5].

584 References

585 Ali, M., Sterk, G., Seeger, M., Stroosnijder, L., 2012. Effect of flow discharge and
586 median grain size on mean flow velocity under overland flow. Journal of
587 Hydrology,452-453,150-160. https://doi.org/10.1016/j.jhydrol.2012.05.051.

588 Ban, Y., Lei, T., Gao, Y., Qu, L., 2017. Effect of stone content on water flow velocity
589 over Loess slope: non-frozen soil. Journal of Hydrology, 549, 525-533.
590 https://doi.org/10.1016/j.jhydrol.2017.03.069.

591 Bouma, T.J., van Duren, L.A., Temmerman, S., Claverie, T., Blanco-Garcia, A.,
592 Ysebaert, T., Herman, P.M.J., 2007. Spatial flow and sedimentation patterns within
593 patches of epibenthic structures: Combining field, flume and modelling
594 experiments. Continental Shelf Research,27(8), 1020-1045.
595 https://doi.org/10.1016/j.csr.2005.12.019.

596 Cao, L., Zhang, K., Dai, H., Liang, Y., 2015. Modeling interrill erosion on unpaved
597 roads in the Loess Plateau of China. Land Degradation & Development,26(8),
598 825-832. https://doi.org/10.1002/ldr.2253.

599 Cen, Y., Zhang, K., Peng, Y., Rubinato, M., Liu, J., Ling, P., 2022. Experimental study
600 on the effect of simulated grass and stem coverage on resistance coefficient of
601 overland flow. Hydrological Processes, 36(10), e14705.
602 https://doi.org/10.1002/hyp.14705.

603 Cen, Y., Zhang, K., Peng, Y., Rubinato, M., Zhang, H., Shang, H., Li, P., 2023.

604 Quantification of the effects on the flow velocity caused by gramineous plants in
605 the loess plateau in North-Western China. Geoderma, 429, 116264.
606 https://doi.org/10.1016/j.geoderma.2022.116264.
607 Cen, Y., Zhang, K., Zhang, M., Zhao, W., Pan, X., Peng, Y., Rubinato, M. 2024. A
608 calculation model of the mean flow velocity of overland flow considering a variety
609 of grass covers and raindrop's characteristics. Soil and Tillage Research. 242,
610 106145. https://doi.org/10.1016/j.still.2024.106145.
611 Chapman, J.A., Wilson, B.N., Gulliver, J.S., 2015. Drag force parameters of rigid and
612 flexible vegetal elements. Water Resources Research,51(5), 3292-3302.
613 https://doi.org/10.1002/2014wr015436.
614 Comiti, F., Mao, L., Wilcox, A., Wohl, E.E., Lenzi, M.A., 2007. Field-derived
615 relationships for flow velocity and resistance in high-gradient streams. Journal of
616 Hydrology,340(1-2),48-62. https://doi.org/10.1016/j.jhydrol.2007.03.021.
617 David, G.C.L., Wohl, E., Yochum, S.E., Bledsoe, B.P., 2010. Controls on spatial
618 variations in flow resistance along steep mountain streams. Water Resources
619 Research,46(3), W03513. https://doi.org/10.1029/2009wr008134.
620 Ding, L., Fu, S., Zhao, H., 2021. Hydraulic properties affected by litter and stem cover
621 under overland flow. Hydrological Processes,35(3), e14088.
622 https://doi.org/10.1002/hyp.14088.
623 Feng, R., Wang, F., Ban, Y., Chen, C., 2020. Method for estimating overland flow
624 velocity on sandified slopes from measured solute transport process with bias

errors. Journal of Hydrology,589, 125116. https://doi.org/10.1016/j.jhydrol.2020.125116.

Ferguson, R., 2010. Time to abandon the Manning equation? Earth Surface Processes and Landforms,35(15),1873-1876. https://doi.org/10.1002/esp.2091.

Ferguson, R.I., 2021. Roughness calibration to improve flow predictions in coarse-bed streams. Water Resources Research,57(6), e2021WR029979. https://doi.org/10.1029/2021wr029979.

Friedrichs, M., Graf, G., Springer, B., 2000. Skimming flow induced over a simulated polychaete tube lawn at low population densities. Marine Ecology Progress Series,192(1),219-228. https://doi.org/10.3354/meps192219.

Fu, S., Mu, H., Liu, B., Yu, X., Liu, Y., 2019. Effect of plant basal cover on velocity of shallow overland flow. Journal of Hydrology,577,123947. https://doi.org/10.1016/j.jhydrol.2019.123947.

Giménez, R., Govers, G., 2001. Interaction between bed roughness and flow hydraulics in eroding rills. Water Resources Research,37(3),791-799. https://doi.org/10.1029/2000wr900252.

Govers, G., 1992. Relationship between discharge, velocity and flow area for rills eroding loose, non‐layered materials. Earth Surface Processes and Landforms,17(5),515-528. https://doi.org/10.1002/esp.3290170510.

Han, D., Deng, J., Gu, C., Mu, X., Gao, P., Gao, J. 2021. Effect of shrub-grass vegetation coverage and slope gradient on runoff and sediment yield under

646 simulated rainfall. International Journal of Sediment Research, 36(1), 29-37.
647 https://doi.org/10.1016/j.ijsrc.2020.05.004
648 Helmers, M.J., Eisenhauer, D.E., 2006. Overland flow modeling in a vegetative filter
649 considering non-planar topography and spatial variability of soil hydraulic
650 properties and vegetation density. Journal of Hydrology,328(1-2),267-282.
651 https://doi.org/10.1016/j.jhydrol.2005.12.026.
652 Hessel, R., Jetten, V., Guanghui, Z., 2003. Estimating Manning's n for steep slopes.
653 Catena,54(1-2),77-91. https://doi.org/10.1016/s0341-8162(03)00058-4.
654 Jarrett, R., 1984. Hydraulics of high-gradient streams. Journal of Hydraulic
655 Engineering,110(11), 1519-1539. https://doi.org/10.1061/(ASCE)0733-
656 9429(1984)110:11(1519).
657 Jin, C.X., Römkens, M.J.M., Griffioen, F., 2000. Estimating manning's roughness
658 coefficient for shallow overland flow in non-submerged vegetative filter strips.
659 Transactions of the Asae,43(6),1459-1466. https://doi.org/10.13031/2013.3044.
660 Kim, J., Ivanov, V.Y., Katopodes, N.D., 2012. Hydraulic resistance to overland flow on
661 surfaces with partially submerged vegetation. Water Resources Research 48 (10),
662 W10540. https://doi.org/10.1029/2012wr012047.
663 Kirstetter, G., Hu, J., Delestre, O., Darboux, F., Lagrée, P.Y., Popinet, S., Fullana, J.M.,
664 Josserand, C., 2016. Modeling rain-driven overland flow: Empirical versus
665 analytical friction terms in the shallow water approximation. Journal of
666 Hydrology,536,1-9. https://doi.org/10.1016/j.jhydrol.2016.02.022.

667 Li, G., Abrahams, A.D., 1997. Effect of saltating sediment load on the determination of
668 the mean velocity of overland flow. Water Resources Research,33(2),341-347.
669 https://doi.org/10.1029/96wr02937.
670 Li, J. J., Wang, W. J., Dong, F., Peng, W. Q., Fan, J. J., Zhao, H. Q., Chou, Q. C., Huang,
671 A. P. 2024. New Drag Force Formula of Bending Stems in Deriving Analytical
672 Solutions of Velocity Profile for Flow Through Flexible Vegetation. Water
673 Resources Research, 60(7), e2023WR035951.
674 https://doi.org/10.1029/2023wr035951
675 Li, P., Zhang, K., Xu, Q., Lv, X., Ling, P., Cen, Y., Shang, H. 2022. Experimental study
676 on the correction factor of surface overland flow velocity. Catena, 218, 106576.
677 https://doi.org/10.1016/j.catena.2022.106576
678 Lima, R.L.P.d., Abrantes, J.R.C.B., Lima, J.L.M.P.d., Lima, M.I.P.d., 2015. Using
679 thermal tracers to estimate flow velocities of shallow flows: laboratory and field
680 experiments.Journal of Hydrology and Hydromechanics,63(3):255-262.
681 https://doi.org/10.1515/johh-2015-0028.
682 Liu, H.Q., Yang, J.H., Liu, C.X., Diao, Y.F., Ma, D.P., Li, F.H., Rahma, A.E., Lei, T.W.,
683 2020. Flow velocity on cultivated soil slope with wheat straw incorporation.
684 Journal of Hydrology,584, 124667. https://doi.org/10.1016/j.jhydrol.2020.124667.
685 Liu, C., Zhang, K., Wei, S., Wang, P., Cen, Y., Xia, J. 2023. Evaluation of the effects of
686 grass and shrub cover on overland flow resistance and its attributes under
687 simulated rainfall. Journal of Hydrology, 626, 130285.

https://doi.org/10.1016/j.jhydrol.2023.130285

Mendicino, G., Colosimo, F., 2019. Analysis of flow resistance equations in gravel - bed rivers with intermittent regimes: Calabrian fiumare data set. Water Resources Research,55(8),7294-7319. https://doi.org/10.1029/2019wr024819.

Misraa, R.K., Rose, C.W., 1996. Application and sensitivity analysis of process-based erosion model GUEST. European Journal of Soil Science,47(4),593-604. https://doi.org/10.1111/j.1365-2389.1996.tb01858.x.

Mu, H., Yu, X., Fu, S., Yu, B., Liu, Y., Zhang, G., 2019. Effect of stem cover on hydraulic parameters of overland flow. Journal of Hydrology, 577, 123964. https://doi.org/10.1016/j.jhydrol.2019.123964.

Mügler, C., Planchon, O., Patin, J., Weill, S., Silvera, N., Richard, P., Mouche, E., 2011. Comparison of roughness models to simulate overland flow and tracer transport experiments under simulated rainfall at plot scale. Journal of Hydrology,402(1-2),25-40. https://doi.org/10.1016/j.jhydrol.2011.02.032.

Nearing, M.A., Foster, G.R., Lane, L.J., Finkner, S.C., 1989. A process-based soil erosion model for USDA-water erosion prediction project technology. Transactions of the Asae,32(5),1587-1593. https://doi.org/10.13031/2013.31195.

Nearing, M.A., Polyakov, V.O., Nichols, M.H., Hernandez, M., Li, L., Zhao, Y., Armendariz, G., 2017. Slope–velocity equilibrium and evolution of surface roughness on a stony hillslope. Hydrology and Earth System Sciences,21(6),3221-3229. https://doi.org/10.5194/hess-21-3221-2017.

709 Pan, C., Shangguan, Z., 2006. Runoff hydraulic characteristics and sediment generation
710 in sloped grassplots under simulated rainfall conditions.Journal of
711 Hydrology,331(1-2):178-185. https://doi.org/10.1016/j.jhydrol.2006.05.011.
712 Pan, C., Shangguan, Z., Ma, L., 2015. Assessing the dye-tracer correction factor for
713 documenting the mean velocity of sheet flow over smooth and grassed surfaces.
714 Hydrological Processes,29(26),5369-5382. https://doi.org/10.1002/hyp.10565.
715 Polyakov, V., Nearing, M.A., Stone, J., 2018. Velocities of shallow overland flow on
716 semiarid hillslopes. Earth Surface Processes and Landforms,43(12),2578-2583.
717 https://doi.org/10.1002/esp.4416.
718 Rickenmann, D., Recking, A., 2011. Evaluation of flow resistance in gravel-bed rivers
719 through a large field data set. Water Resources Research,47(7), W07538.
720 https://doi.org/10.1029/2010wr009793.
721 Smith, M. W., Cox, N. J., & Bracken, L. J., 2007. Applying flow resistance equations
722 to overland flows. Progress in Physical Geography, 31(4), 363–387.
723 https://doi.org/10.1177/0309133307081289.
724 Shang, H., Zhang, K., Wang, Z., Yang, J., He, M., Pan, X., Fang, C., 2020. Effect of
725 varying wheatgrass density on resistance to overland flow. Journal of
726 Hydrology,591,125594. https://doi.org/10.1016/j.jhydrol.2020.125594.
727 Shen, E., Liu, G., Jia, Y., Dan, C., Abd Elbasit, M.A.M., Liu, C., Gu, J., Shi, H., 2021.
728 Effects of raindrop impact on the resistance characteristics of sheet flow. Journal
729 of Hydrology,592, 125767. https://doi.org/10.1016/j.jhydrol.2020.125767.

730 Takken, I., Govers, G., Ciesiolka, C.A., Silburn, D.M., Loch, R.J., 1998. Factors
731 influencing the velocity-discharge relationship in rills. Modelling Soil Erosion,
732 Sediment Transport and Closely Related Hydrological Processes,249249:63-69.
733 Takken, I., Govers, G., Jetten, V., Nachtergaele, J., Steegen, A., Poesen, J., 2005. The
734 influence of both process descriptions and runoff patterns on predictions from a
735 spatially distributed soil erosion model. Earth Surface Processes and
736 Landforms,30(2):213-229. https://doi.org/10.1002/esp.1176.
737 Tang, H., Tian, Z., Yan, J., Yuan, S., 2014. Determining drag coefficients and their
738 application in modelling of turbulent flow with submerged vegetation. Advances
739 in Water Resources,69,134-145. https://doi.org/10.1016/j.advwatres.2014.04.006.
740 Tanino, Y., Nepf, H.M., 2008. Laboratory investigation of mean drag in a random array
741 of rigid, emergent cylinders. Journal of Hydraulic Engineering,134(1),34-41.
742 https://doi.org/10.1061/(ASCE)0733-9429(2008)134:1(34).
743 van Wesenbeeck, B., Van De Koppel, J., M. J. Herman, P., J. Bouma, T., 2008. Does
744 scale-dependent feedback explain spatial complexity in salt-marsh ecosystems?
745 Oikos,117(1),152-159. https://doi.org/10.1111/j.2007.0030-1299.16245.x.
746 Wang, W.J., Huai, W.X., Thompson, S., Katul, G.G., 2015. Steady nonuniform shallow
747 flow within emergent vegetation. Water Resources Research 51 (12), 10047–
748 10064. https://doi.org/10.1002/2015wr017658.
749 Wei, S. E., Zhang, K., Liu, C., Cen, Y., Xia, J. 2024. Effects of different vegetation
750 components on soil erosion and response to rainfall intensity under simulated

751 rainfall. Catena, 235, 107652. https://doi.org/10.1016/j.catena.2023.107652

752 Wu, B., Wang, Z., Zhang, Q., Shen, N., Liu, J., 2017. Modelling sheet erosion on steep
753 slopes in the loess region of China. Journal of Hydrology,553,549-558.
754 https://doi.org/10.1016/j.jhydrol.2017.07.017.

755 Yang, C., Sun, X., Yang, Q., Cen, Y., Liu, C., Wei, S., Zhang, K. 2024. Effects of grass-
756 shrub vegetation and litter on overland flow resistance coefficients. Physics of
757 Fluids, 36(10), 103606. https://doi.org/10.1063/5.0232920

758 Yang, P., Zhang, H., Wang, Y., Wang, Y., Wang, Y., 2020. Overland flow velocities
759 measured using a high-resolution particle image velocimetry system. Journal of
760 Hydrology,590,125225. https://doi.org/10.1016/j.jhydrol.2020.125225.

761 Zhang, K., Wang, Z., Wang, G., Sun, X., Cui, N., 2017. Overland-flow resistance
762 characteristics of nonsubmerged vegetation. Journal of Irrigation and Drainage
763 Engineering,143(8):04017021. https://doi.org/10.1061/(asce)ir.1943-
764 4774.0001196.

765 Zhang, M., Zhang, K., Cen, Y., Wang, P., Xia, J. 2025. Effects of grass cover on the
766 overland soil erosion mechanism under simulated rainfall. Water Resources
767 Research, 61(2), e2023WR036888. https://doi.org/10.1029/2023wr036888

768 Zhang, T., Cen, Y., Zhou, K., Zhong, L., Zhou, Y., Ma, G. 2025. Effects of hillside grass
769 distribution patterns on soil erosion and the particle size distribution of sediments
770 under different rainfall intensities. Hydrological Processes, 39(1).
771 https://doi.org/10.1002/hyp.70057

772 Zhang, Y., Wang, P., Cheng, J., Wang, W.J., Zeng, L., Wang, B., 2020. Drag Coefficient
773 of Emergent Flexible Vegetation in Steady Nonuniform Flow. Water Resources
774 Research,56(8), e2020WR027613. https://doi.org/10.1029/2020wr027613.
775 Zhang, H.Y, Zhang, K. D, Liu, L.L, Wang, M., Cen, Y.D., 2022a. Quantifying the effects
776 of grass distribution patterns on the relative hydrodynamic parameters of overland
777 flow. Hydrological Processes, 36 (10), e14707. https://doi.org/10.1002/hyp.14707.
778 Zhang, J., Zhang, S., Wang, C., Wang, W., & Ma, L. 2022b. Influence of combined stem
779 vegetation distribution and discretization on the hydraulic characteristics of
780 overland flow. Journal of Cleaner Production, 376(13), 134188.
781 https://doi.org/10.1016/j.jclepro.2022.134188.
782 Zhang, R., Zheng, C. J., Zhu, D. L., Wu, P. T., Liu, Y. C., Zhang, X. M., Khudayberdi,
783 N., & Liu, C. X. (2023). Variation in sprinkler irrigation droplet impact angle on
784 the physical crusting properties of soils. Agricultural Water Management, 289,
785 108514. https://doi.org/10.1016/j.agwat.2023.108514.
786 Zhao, W., Zhang, K., Cen, Y., Hu, W., Yang, C., Yang, Q. 2025. Response law and
787 prediction model of soil erosion considering vegetation and litter cover under
788 different rainfall intensities in the Loess Plateau. Soil and Tillage Research, 251,
789 106559. https://doi.org/10.1016/j.still.2025.106559.
790 Zong, L., Nepf, H., 2010. Flow and deposition in and around a finite patch of vegetation.
791 Geomorphology,116(3-4):363-372.
792 https://doi.org/10.1016/j.geomorph.2009.11.020.